Surface & Coatings Technology 485 (2024) 130891

Contents lists available at ScienceDirect

Surface & Coatings Technology

journal homepage: www.elsevier.com/locate/surfcoat

Full Length Article

Nanocrystalline Y_2O_3-modified metal matrix composite coatings with improved resistance to thermocyclic oxidation and V_2O_5-induced type II hot corrosion

Christoph Grimme [a,*], Kan Ma [b,*], Robin Kupec [a], Ceyhun Oskay [a], Emma M.H. White [a], Alexander J. Knowles [b], Mathias C. Galetz [a]

[a] DECHEMA-Forschungsinstitut, Theodor-Heuss-Allee 25, 60486 Frankfurt am Main, Germany
[b] University of Birmingham, School of Metallurgy and Materials, Birmingham B15 2TT, United Kingdom

ARTICLE INFO

Keywords:
Metal matrix composite
Co-electrodeposition
Diffusion coatings
Interdiffusion
Corrosion inhibition
Oxidation

ABSTRACT

Incorporating reactive elements (RE) into turbine coatings is a well-established surface treatment. However, suboptimal RE concentrations can lead to compromised strength, heightened brittleness, and reduced adhesion. In contrast, RE oxides offer advantages of avoiding these detrimental effects, counteracting corrosion phenomena induced by V_2O_5 compounds and enhancing oxidation resistance. A notable challenge lies in optimizing RE oxide particle incorporation and understanding the influence of particles in coating microstructures. This study focuses on developing Ni—Al and Ni-Cr-Al type metal matrix composite (MMC) coatings on Inconel 617 (IN617), containing up to 11 vol% of Yttria (Y_2O_3) nanoparticles. Y_2O_3 nanoparticles and Ni were co-electrodeposited on IN617 followed by either pack aluminizing or a two-step chromizing and aluminizing process. An even distribution of Y_2O_3 nanoparticles was observed throughout the entire 100 µm coating thickness, leading to significant grain refinement in the sub-micron to nano range in both coating types. Y_2O_3-strengthened coatings were subjected to oxidation at 1100 °C and hot corrosion at 700 °C and were compared to their Y_2O_3-free counterparts. Present at grain boundaries, Y_2O_3 markedly enhanced the oxidation and corrosion resistance by reducing interdiffusion, improving the oxide scale adherence and binding V_2O_5, highlighting the potential of this method for advanced turbine blade coatings.

1. Introduction

Nickel-based alloys exhibit excellent creep and fatigue strength, and thus, are commonly used in aerospace and land-based gas turbines. Stationary gas turbines for power generation often run on low cost, low-grade fuels with high impurities, such as vanadium, to ensure the economical operation of the plant [1]. The presence of vanadium impurities causes high amounts of ash to form during combustion, accelerating high-temperature corrosion by dissolving otherwise protective oxide scales on the turbine blades [2–5]. Vanadium increases corrosion because it forms a low-melting, highly corrosive eutectic between Na_2SO_4 and V_2O_5 with a melting point of 525 °C. So far, one of the most effective methods to inhibit this vanadium-induced low-temperature hot corrosion (LTHC) is to add Mg in a fuel-soluble form, such as magnesium naphthenate ($C_{22}H_{14}MgO_4$). Mg triggers a strong acid/base reaction between the inhibitor and vanadium in the combustion gas [6]. The added inhibitors react with V_2O_5 in the combustion gas [7] to form higher melting point compounds, which prevents the formation of the low-melting, highly corrosive Na_2SO_4 and V_2O_5 eutectic. Preventing the formation of a molten ash deposit slows down the ion exchange between the combustion gas and structural materials, and thereby lowers the corrosive attack. The positive influence of Mg- and/or Ca-compound fuel additions on reducing the V_2O_5-Na_2SO_4 corrosion has been shown by several authors [8–10]. Unfortunately, these higher melting point compounds deposit as slags on colder parts of the turbine, such as the blades, and regular downtimes are required to remove these deposits and ensure the effectiveness of the plant [11]. Considering the corrosion and interaction mechanisms, corrosion inhibitors within a protective coating would be an efficient way to reduce or avoid these fuel additions and the resulting undesirable deposits and associated plant downtimes.

Diffusion coatings manufactured by the pack cementation method have evolved as state-of-the-art coatings due to their high oxidation and

* Corresponding authors.
E-mail addresses: christoph.grimme@dechema.de (C. Grimme), k.ma@bham.ac.uk (K. Ma).

https://doi.org/10.1016/j.surfcoat.2024.130891
Received 26 February 2024; Received in revised form 18 April 2024; Accepted 6 May 2024
Available online 8 May 2024

corrosion resistance and relatively low-cost manufacturing process when compared to other coating deposition techniques such as high-velocity oxy-fuel (HVOF) or atmospheric plasma spraying (APS) [12]. Also diffusion coatings could potentially have even better oxidation and corrosion resistance through the "reactive element effect" [13–15], if small amounts of reactive elements or ceramic particles were able to be incorporated. The "reactive element effect" [13–15] promotes the formation of an adherent and protective oxide scale.

However, two challenges exist in creating particle-strengthened diffusion coatings. First, there is a limited ability to integrate ceramic particles into a dense diffusion coating using pack cementation [16], achieving the necessary thickness of around 100 μm for effective corrosion inhibition in turbine applications. This limitation could be overcome if the particles were applied before the pack cementation process. Galvanic coating production was selected since the synthesis of nano-particle-reinforced materials by conventional casting methods is not possible due to the low wettability of nanoparticles by molten metal [21]. Second, the selection of particles in combination with the pre-application process is imperative to achieve a dense and protective coating. The main particles of interest for inhibiting vanadium-sodium sulfate-induced hot corrosion would be magnesium and calcium compounds since they react with vanadium and prevent the formation of low melting eutectics between vanadium oxide and sodium sulfates [6,7,9,17]. However, for a low cost preapplication of the particles, such as galvanic co-deposition in aqueous acidic media, most Mg and Ca inhibitor compounds are ineligible. Oxides of calcium and magnesium strongly affect pH by a reaction with water according to Eqs. (1.1) and (1.2), respectively.

$$MgO_{(s)} + H_2O_{(l)} \rightarrow Mg(OH)_{2(aq)} \quad (1.1)$$

$$CaO_{(s)} + H_2O_{(l)} \rightarrow Ca(OH)_{2(aq)} \quad (1.2)$$

Adding these reactive basic oxides to an industrial acidic electrolyte for nickel plating would alter the optimum pH value of sulfamate electrolytes, ranging from a pH of 3.5–4 [18,19], to above 5. At pH values above 5, the precipitation of nickel(II) hydroxide begins [19], depositing within the electroformed metallic nickel layer, causing embrittlement and "burned" nickel layers with a dark appearance [19]. The potential inhibitors are therefore limited, since there are few commercially available magnesium or calcium compounds with a chemical stability in the pH range between 3 and 5.

The significance of zeta potential as an additional crucial selection criterion becomes evident when examining Fig. 1. A strong positive zeta potential is instrumental in achieving favorable floating and co-deposition behaviors and induces electrophoretic migration towards the cathode, the target surface for coating. Additionally, the particles must be of micro- or nano-size to prevent gravitational sedimentation, as emphasized by Schwegmann et al. [20], further limiting the commercially available materials [21].

As an alternative to Mg and Ca, Y_2O_3 could potentially exhibit a similar corrosion resistance effect on vanadate corrosion. Yttria can form the compound YVO_4, which has an elevated melting point of 1810 °C [22]. Additionally, the zeta potential of yttria has been demonstrated to fall within a significantly positive range by several authors [23–25], rendering yttria highly suitable for co-electroplating in an acidic electrolyte. Therefore, commercially available yttria nanoparticles were selected for the co-deposition by electroplating.

Based on the forementioned challenges, this work developed a metal matrix composite (MMC) coating deposited by electroplating to incorporate greater amounts of potential vanadium inhibitors (Y_2O_3) for improved oxidation and corrosion resistance. After electroplating, the deposited Ni-Y_2O_3 coatings were enriched with chromium and aluminum via pack cementation. In this study, the two new coating manufacturing processes are described to achieve corrosion- and oxidation-resistant coatings with incorporated oxide nanoparticles. The oxidation and vanadate corrosion resistance of the MMC coatings were investigated, and their respective microstructural features were characterized and discussed.

2. Experimental procedures

2.1. Sample preparation and electroplating

IN617 samples (VDM Metals GmbH) with dimensions of 15 × 6 × 6 mm^3 were manufactured by electric arc wire cutting. These samples underwent further preparation, including grinding with P320 grit SiC paper and subsequent ultrasonic cleaning using acetone. Before coating application surface activation was required to improve surface adhesion of the electroplated functional inhibitor coating and to prevent blistering during the subsequent heat treatment steps. Surface activation was performed immediately after grinding using Ni-Strike (150 g/l $NiCl_2$ x 6 H_2O, 50 ml/l HCl 32 %) at room temperature. The Ni-strike electrolyte was kept at a pH of 1 while being agitated at 400 rpm. A soluble Ni anode was used for this process at a current density of 5 A/dm^2 for a duration of 300 s.

After the surface activation, the samples were immersed in a nickel sulfamate bath (300 g/l Ni-sulfamate, 30 g/l boric acid) which was kept between a pH of 3 and 4. The immersion was conducted without rinsing in deionized water after Ni-strike to prevent passivation and contamination of the activated surface. The coating deposition in the Ni-sulfamate electrolyte was performed for a duration of 2 h using direct

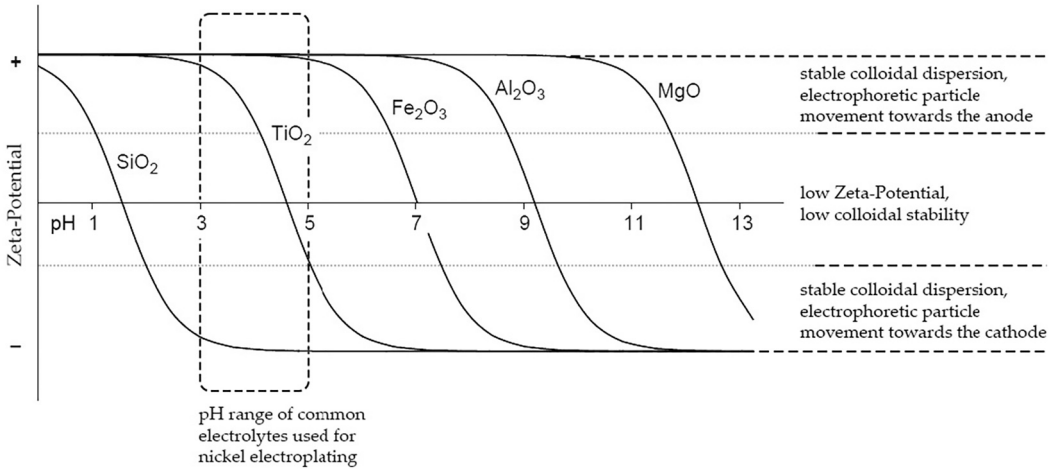

Fig. 1. Schematic drawing of the pH-dependent Zeta potential for different particle types, after [18].

current (DC) in combination with dimensionally stable anodes (DSAs) at a cathodic current density of 3 A/dm^2 at 45 °C in an ultrasonic bath (Elmasonic S, Elma Schmidbauer GmbH) using ultrasonic sweep mode (80 W; 320 W max.). For the deposition of the Ni-Y_2O_3 inhibitor coatings, 10 g/l yttria nanopowder (chemPUR) with an average particle size between 30 and 50 nm was added to the Ni-sulfamate electrolyte. The galvanic deposition setup for the coatings is shown schematically in Fig. 2.

DSAs were used to lower the pH-level of the Ni-sulfamate electrolyte during the coating deposition. Nickel carbonate was added after the deposition processes to raise the pH-level and increase the concentration of nickel ions at the same time without adding unwanted substances such as chlorides (e.g. HCl), which are typically required when using soluble anodes.

2.2. Diffusion coatings on the deposited Ni-Y_2O_3 MMC-layers

Two different pack cementation mixtures were used for the different diffusion coatings on the Ni-Y_2O_3 MMC coating. Aluminizing carried out on the electroplated coating led to the formation of a Ni-Y_2O_3-Al coating. A two-step-process, where the aluminizing step followed an initial chromizing process led to the formation of a Ni-Y_2O_3-Cr-Al coating. The pack mixtures consisted of master alloys of 20 wt% Cr for chromizing or 20 wt% Al for aluminizing, 1 wt% NH_4Cl halide activator and 79 wt% Al_2O_3 inert filler. High contents of the master alloys were chosen to ensure high diffusion into the substrate. The samples were placed inside alumina crucibles which were filled with the pack mixture. The pack cementation was conducted in a horizontal quartz tube furnace at 1050 °C for chromizing and 800 °C for aluminizing for 4 h under flowing (4 l/h) Ar + 5 vol% H_2.

2.3. Oxidation and corrosion testing

Thermocyclic oxidation tests were conducted at a dwell temperature of 1100 °C for up to 300 cycles, with a cycle duration of 67 min to ensure 1 h exposure at 0.97 T_{dwell}, following ISO13573:2012 [26]. Between the hot dwell of each cycle, the samples were cooled down below 50 °C using pressurized air cooling (PAC) for 15 min. The occurring mass changes were measured every 20 h using a high precision balance (XP205DR, Mettler-Toledo). To analyze the simultaneous microstructural changes occurring due to diffusion, isothermal exposures at 1100 °C up to 500 h were also carried out. Additionally, quasi-isothermal oxidation was conducted at 1100 °C for up to 500 h with furnace cooling every 100 h for determination of the mass changes. Vanadate hot corrosion was investigated by applying 30 mg/cm^2 of a 60V_2O_5-40Na_2SO_4 salt mixture (homogenized at 900 °C in a covered quartz crucible) on the coatings and placing them in a horizontal tube furnace at 700 °C for 50 h in synthetic (syn.) air +0.1 vol% SO_2. Furthermore, one sample of IN617 was deeply embedded in a mixture of 60V_2O_5-40Na_2SO_4 wt%, while another one was embedded into the same mixture, but with yttria added in a stoichiometric ratio to the vanadate component. Both samples were placed in the previously mentioned furnace under identical atmospheric conditions. This investigation was conducted to assess the impact of yttria on corrosion in comparison to a salt mixture lacking yttria.

2.4. Analytical characterization

The coated surfaces were analyzed using optical microscopy (OM). Additionally, cross-sections were prepared using standard metallographic methods including wet grinding with SiC paper and polishing with diamond suspensions down to 1 µm. Changes in microstructure and phase compositions after deposition, oxidation and corrosion tests were analyzed using OM, scanning electron microscopy (SEM/EDS) (FlexSEM 1000 II, Hitachi) and electron probe microanalysis (EPMA) (JXA-8100 EPMA, Jeol). Crystallographic phase identification was conducted using X-ray diffraction (XRD) (D8 Advance, Bruker). For grain size analysis electron backscatter diffraction (EBSD) (FE-SEM SU5000, Hitachi) was carried out. The depth of the corrosion attack was measured visually with respect to the initial coating or sample thickness across the sample surface using a grid with a grid distance of 100 µm in ImageJ2/Fiji. Over 70 measurements were sorted according to their corrosion depth and then plotted in a cumulative probability plot [27–29] to show the overall corrosion attack. Transmission electron microscopy (TEM) was used to study the distribution of yttria nanoparticles. TEM samples were lifted out from the Ni-Y_2O_3-Al coating using a focused ion beam (FIB) equipped on an FEI Quanta 3D dual-beam SEM. TEM and scanning transmission electron microscopy (STEM) characterization with STEM/EDS was performed using an FEI Talos F200X TEM operated at 200 kV. STEM-high angle annular dark field (HAADF) images were taken with a collection angle of 18–110 mrad with which both diffraction contrast and mass contrast were present.

3. Results and discussion

3.1. Characterization of coating microstructures and influence of pack diffusion activity on element distribution

Due to the high surface-to-volume ratio of nanoparticles, agglomerates tend to form rather than an even dispersion for electroplating. By combining electrodeposition with ultrasound (US) rather than conventional stirring, agglomeration between particles could be reduced. Co-

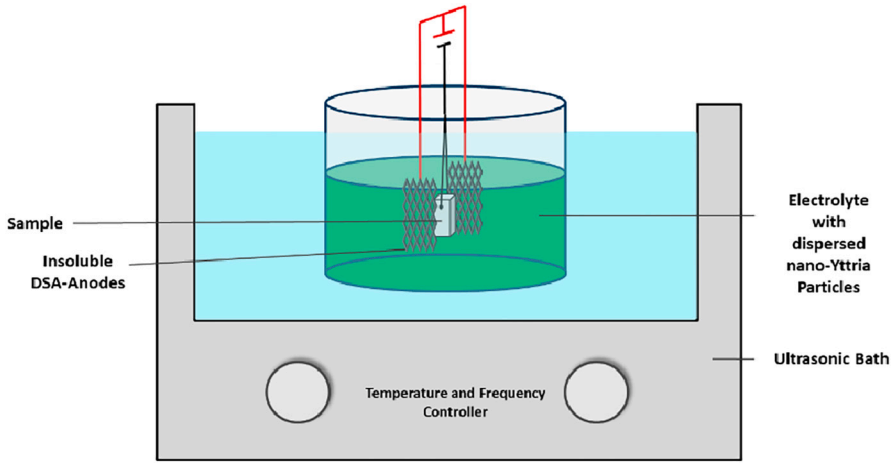

Fig. 2. Schematic drawing of the co-deposition process conducted in an ultrasonic bath with insoluble DSAs.

deposition using US also promoted greater particle incorporation of 11 vol% and resulted in a uniform dispersion of particles across all surfaces [30–33] and led to coating thicknesses of around 55 µm. The cross-sections of the resulting Ni-Y_2O_3 coatings are shown in Fig. 3 and were subsequently used in the pack cementation processes.

After the pack cementation process, several changes regarding the distribution of the particles in the coating were observable, depending on the activity of the diffusing element in the pack mixture and in the substrate. Furthermore, differences in coating thickness were observed between particle-free and particle-containing coatings, as illustrated by the comparison between Ni—Al and Ni-Y_2O_3-Al coatings in Fig. 4a and b, as well as between Ni-Cr-Al and Ni-Y_2O_3-Cr-Al coatings in Fig. 5a and b. The presence of particles in the Ni-Y_2O_3-Al coatings (Fig. 4b) led to a reduction in coating thickness by approximately 15 µm compared to the particle-free Ni—Al coatings (Fig. 4a). On the contrary, the presence of particles in the Ni-Y_2O_3-Cr-Al coatings (Fig. 5b) resulted in an approximate 10 µm increase in coating thickness compared to the particle-free Ni-Cr-Al coatings (Fig. 5a).

Aluminum diffusion mainly proceeded via the inward diffusion of Al due to the high activity of Al in the pack mixture. Consequently, the distribution of particles remained uniformly dispersed, albeit with a minor decline in particle density observed from the upper to lower Al-enriched coating regions, as depicted in Fig. 4b. With a homogenous Al content of around 60 at.%, an intermetallic δ-Ni_2Al_3 coating of around 100 µm formed. However, since the formation of Ni_2Al_3 from Ni was accompanied by an increase in volume due to the uptake of Al into the Ni matrix, the particle density in the intermetallic matrix decreased (Fig. 4b) compared to the as-deposited Ni-Y_2O_3 coating depicted in Fig. 3. Beneath the intermetallic δ-Ni_2Al_3 coating, a small interdiffusion zone of around 5 µm consisted of β-NiAl and γ-Ni_3Al, which were determined by the elemental compositions from SEM (EDS) and EPMA (line-scan) measurements. Underneath the intermetallic phases the Y concentration remained the same as the initial concentration of the as-deposited Ni-Y_2O_3 layer (Fig. 3).

For the Ni-Y_2O_3-Cr-Al coatings formed by low-activity Cr pack cementation with subsequent high-activity Al pack cementation shown in Fig. 5b, the outward diffusion of Ni was predominant and led to the formation of three different intermetallic zones on top of the initial electroplated Ni-Y_2O_3 coating (Fig. 5b). Zone 1 was around 15 µm in thickness and was identified as an intermetallic δ-Ni_2Al_3 matrix with a high Al content of up to 76 at.% and a high Cr content between 10 and 17 at.%. Zone 2 was divided into two subzones, namely 2a and 2b, which differed in their Cr content. Zone 2a with a thickness of around 40 µm consisted of a δ-Ni_2Al_3 matrix with a high density of Cr-rich precipitates, most likely α-Al_8Cr_5. The composition matched the α-Al_8Cr_5 phase which is present according to the ternary Al-Cr-Ni diagram at 700 °C [34,35]. Slurry aluminization experiments on Ni—20Cr substrates conducted by Grégoire et al. [36] showed similar precipitates. Zone 2b with a thickness of around 15 µm did not show any Cr-rich precipitates. High concentrations of Y and Cr were measured throughout Zone 3, which consisted of β-NiAl. The highest concentrations of Y could be found in the region of the electroplated Ni-Y_2O_3 layer, which showed even higher levels of Y than in the as-electroplated condition. Since the Ni matrix diffused outwards during Cr pack cementation, the particles became concentrated in this layer. Compared to the particle-free coatings depicted in Fig. 5a, the Ni-Y_2O_3-Cr-Al coatings exhibit a notable enrichment in chromium within the γ-Ni phase (Fig. 5b). In contrast, the Ni-Cr-Al coatings do not show a significant chromium reservoir beneath the intermetallic phases (Fig. 5a). The particle-free coatings present a comparable zonation to the Ni-Y_2O_3-Cr-Al coatings, albeit with differences in the thicknesses of the respective zones as well as the chromium concentration. Generally, the thicknesses of all zones are smaller; however, the chromium concentration in the uppermost zones 1 and 2a is slightly higher, reaching concentrations of up to 33 at.%.

The influence of the Y_2O_3-particles on the microstructure after Al pack cementation is shown in Fig. 6. Aluminum diffusion coatings on galvanically deposited Ni (Fig. 6a) showed a coarse-grained microstructure after the Al diffusion coating. The incorporation of Y_2O_3 into the galvanic Ni coating decreased the average grain size remarkably (Fig. 6b) after the Al diffusion coating. At the surface of the coating, the grains exhibited a submicron size. The average grain size gradually increased with the depth under the coating surface, reaching their largest size at the interface between the substrate and the coating. This observed increase in the grain size aligns with the slight reduction in the Y content, as illustrated in Fig. 4. Consequently, this phenomenon can be plausibly attributed to the grain boundary pinning effect caused by the presence of Y_2O_3 nanoparticles.

A similar grain-refining effect was observed in the case of the Ni-Y_2O_3-Cr-Al coating, with aluminization following chromizing (as shown in Fig. 6c). It is worth noting that the grain refinement was also evident in the region without particles (Zone 1 and 2 in Fig. 5, visible in in Fig. 6c). This effect was attributed to the precipitation of chromium-aluminides, which occurred during the final aluminum pack cementation step of the process. Notably, the intermediate layer (Zone 2b) of the coating, which was both particle- and precipitation-free, exhibited a similar grain size to that of the unmodified Ni—Al coating, as can be seen in both Fig. 6a and c. However, in the particle-enriched layer adjacent to the substrate (Fig. 6c) a significant grain refinement was again observable. In addition, this substrate interface layer showed Kirkendall voids from Ni outward diffusion.

Fig. 7 compares the initial Al-uptake during the pack cementation process. Interestingly, despite having significantly larger grain sizes, the particle-free Ni—Al coatings exhibit higher Al-uptake compared to the particle-containing Ni-Y_2O_3-Al coatings, which have noticeably smaller

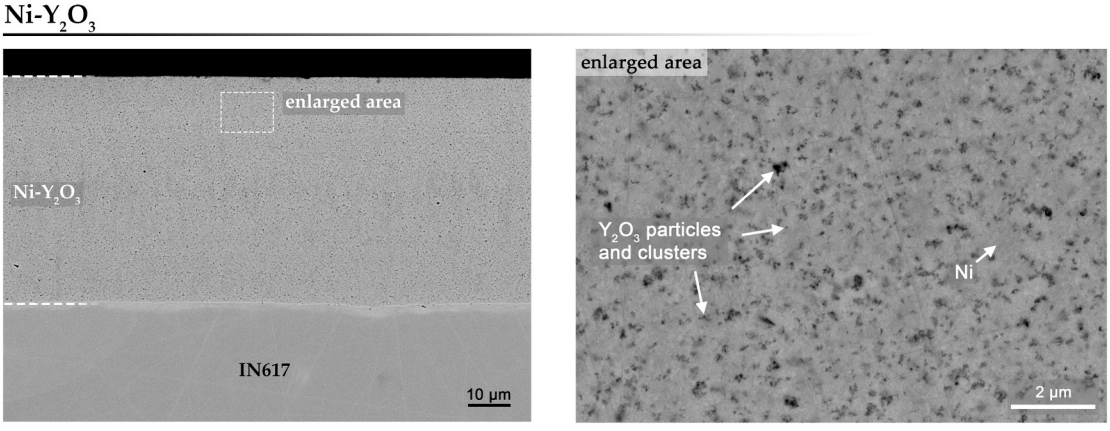

Fig. 3. SEM-BSE cross-sectional image of the Ni-Y_2O_3 MMC coating after co-deposition in a Ni-sulfamate electrolyte using DSAs in combination with US.

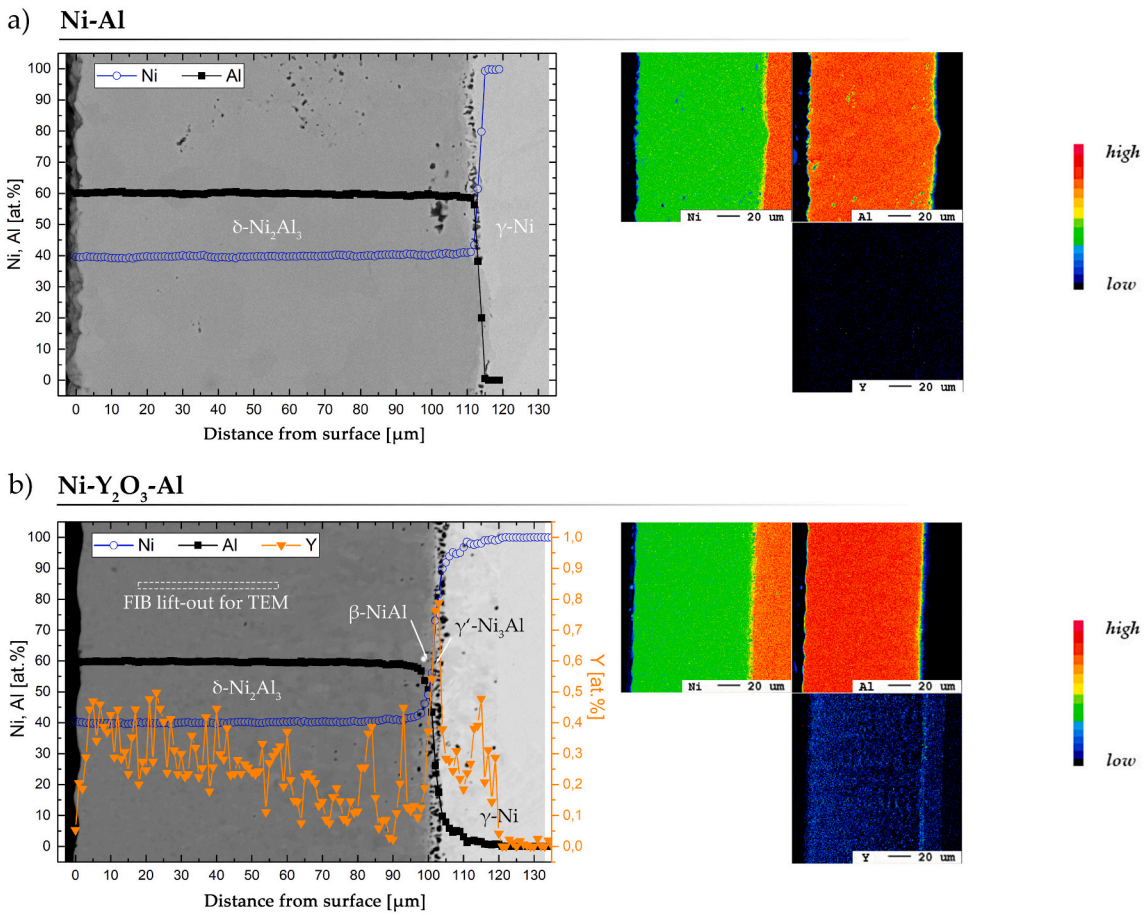

Fig. 4. SEM-BSE image of: a) Ni-Al coating and b) Ni-Y_2O_3-Al coating with a line scan through the surface cross-section and the respective EPMA element distribution maps.

grain sizes. While diffusion is normally faster at grain boundaries due to a high number of vacancies, an opposite finding was expected. However, when the Cr pack cementation process was performed prior to the aluminization process, the presence of Y_2O_3 particles not only resulted in an increased chromium uptake but also led to an increased aluminum uptake during the subsequent aluminization process. The aluminum pack cementation after chromizing led to the formation of Ni_2Al_3 with Cr—Al precipitates, where the precipitates promoted an increase of the mean Al-concentration from 60 at.% to around 70 at.% (see Figs. 4 and 5). As the resulting Ni-Y_2O_3-Cr diffusion coating was thicker for particle-containing coatings, a following aluminization process may then also cause a higher aluminum uptake. These effects could be related to the distribution of yttria particles which requires further investigation.

3.2. Investigation of yttria particle distribution

To provide a more comprehensive understanding of the effect of nanoparticle distribution on the coating microstructure, a thorough characterization of the Ni-Y_2O_3-Al coating was performed using TEM, as evident from the highlighted lift-out area in Fig. 4. This TEM lamella, shown in Fig. 8 with an enlarged view, reveals a high concentration of Y_2O_3 particles located both within the grains and at or in proximity to grain boundaries. Within the grains, dislocation lines were tangled with the nanoparticles.

The presence of particles caused significant grain refinement during the high activity Al pack cementation for the Ni-Y_2O_3-Al coating when compared to coatings without particles [37–40]. Fine-grained materials typically exhibit enhanced inward diffusion of aluminum, as diffusion should be faster for nano-sized grains compared to micro-sized grains, higher versus lower grain boundary densities, respectively [41]. At 800 °C, the grain boundaries were shown to be the main diffusion pathway for aluminum in Ni—Al [42]. Thus, these Ni-Y_2O_3-Al coatings, exhibiting substantial grain refinement, presents a behavior contrary to what is typically documented in the literature: Al diffusion was reduced from the presence of Y_2O_3 nanoparticles despite grain refinement resulting in a higher density of grain boundaries.

This positioning of the particles at grain boundaries, as confirmed in another magnified region in Fig. 9, likely impeded the movement of grain boundaries and grain growth during the pack cementation process. A notable indication of the constrained grain boundary mobility can be observed in the presence of twisted grain boundaries, as depicted in Fig. 9. It is evident that these distorted grain boundaries are closely associated with the presence of Y_2O_3 in these regions. Furthermore, it is worth noting that particles have a known inhibitory effect on the diffusion of aluminum along grain boundaries at elevated temperatures, as established in previous research by Geers et al. [43]. This hindrance is particularly significant because grain boundary diffusion is a well-documented dominant mechanism for aluminum diffusion, especially up to 1100 °C, as demonstrated by Janssen et al. [42]. Consequently, this is a plausible explanation for the reduced uptake of aluminum in coatings containing these particles during the Al-pack cementation process.

Although this hindrance should theoretically decrease the outward diffusion of Ni to combine with Cr from the gas phase during Cr pack cementation, the opposite is observed. This apparent contradiction can be elucidated by considering the reduction and distribution of Kirkendall voids facilitated by the particles, which act as vacancy sinks [44]. Consequently, with less vacancies and either fewer or more evenly distributed Kirkendall voids, there is a slower yet continuous diffusion of

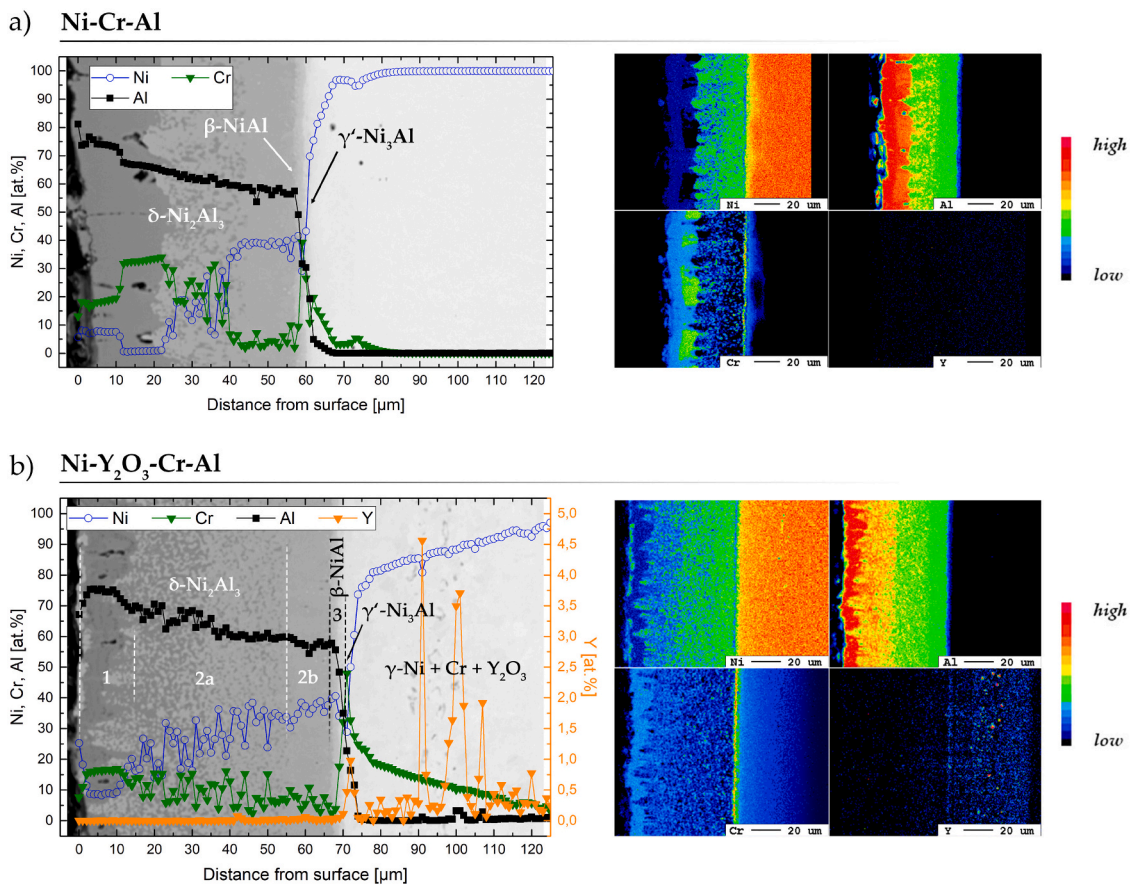

Fig. 5. SEM-BSE image of: a) Ni-Cr-Al coating and b) Ni-Y_2O_3-Cr-Al coating with a line scan through the surface cross-section and the respective EPMA element distribution maps.

Ni, enabling higher coating thicknesses during Cr pack cementation compared to particle-free coatings.

3.3. Vanadate inhibition potential by yttria

The two samples of IN617 that were deep embedded into a 60V_2O_5-40Na_2SO_4 salt mixture with and without yttria inhibitor revealed significant differences regarding the corrosion attack. While the sample immersed in the ash mixture (60V_2O_5-40Na_2SO_4) without inhibitor showed heavy corrosion, no signs of accelerated corrosion could be observed on the sample immersed in an inhibitor-ash mixture (60V_2O_5-40Na_2SO_4 + Y_2O_3). XRD of the 60V_2O_5-40Na_2SO_4 + Y_2O_3 (Fig. 10) after exposure at 700 °C for 50 h in a syn. Air +0.1 vol% SO_2 atmosphere showed a complete conversion of V_2O_5 and Y_2O_3 to YVO_4, which has a melting point of around 1810 °C [22]. At the test temperature of 700 °C, the conversion of vanadium pentoxide to yttrium vanadate took place, consistent with Chen et al. [45]. This confirmed the selective reaction of vanadium pentoxide by yttria inhibitors, effectively mitigating the corrosion of IN617 deeply embedded within the 60V_2O_5-40Na_2SO_4 + Y_2O_3 mixture.

3.4. Improved oxidation resistance via yttria at 1100 °C

Oxide scales that develop on metallic surfaces are commonly prone to inherent growth stresses, which, when they reach a critical threshold, can result in scale failure, including spallation or the formation of cracks [46]. Furthermore, variations in temperature, such as the cooling process during thermocyclic tests, have the potential to increase the stress within the oxide scale from the mismatch in thermal expansion coefficients (CTE) between the scale and the substrate [47]. Such a disparity can result in a greater tendency for scale spallation during exposure, particularly when compared to isothermal exposure conditions, ultimately leading to an accelerated depletion of the oxide-forming elements. The formation of fast-growing transient oxides can occur when the protective oxide former is critically depleted, further increasing spallation and leading to drastic negative net mass changes [48].

During cyclic oxidation tests of these MMC coatings conducted at 1100 °C with PAC applied between the cycles, a significant change in oxidation resistance was observed, primarily attributable to the presence of dispersed yttrium oxide particles (Fig. 12). As a reference, uncoated IN617 (Fig. 11a) showed mass loss after 80 cycles indicating characteristic chromia spallation [49]. Al diffusion-coated IN617 (Fig. 11a) showed a negative mass change after only 20 to 40 cycles, also due to significant oxide spallation [50]. The Ni-electroplated and aluminized (Ni—Al) showed high oxidation rates accompanied by spallation after 220 cycles (Fig. 11b). Chromized and aluminized coatings (Ni-Cr-Al) showed a linear mass loss starting after just 20 cycles (Fig. 11c). The addition of yttria nanoparticles led to a significant improvement in the oxidation resistance for both coating types (Fig. 11b and c). The Ni-Y_2O_3-Al coating showed continuous protection against oxidation even after 300 cycles, visible by the extremely low mass gain. The Ni-Y_2O_3-Cr-Al coating also strongly improved the oxidation resistance with a slight positive mass gain still observable after 280 cycles [51–53].

Cross-sections of the oxidized coated samples after 300 cycles were analyzed using SEM and EPMA. Fig. 12 presents the Ni—Al and Ni-Y_2O_3-Al coating cross-sections and elemental concentration profiles. The Ni—Al coating (Fig. 12a) showed extensive formation of Kirkendall voids at the substrate-coating interface, which coalesced due to the high

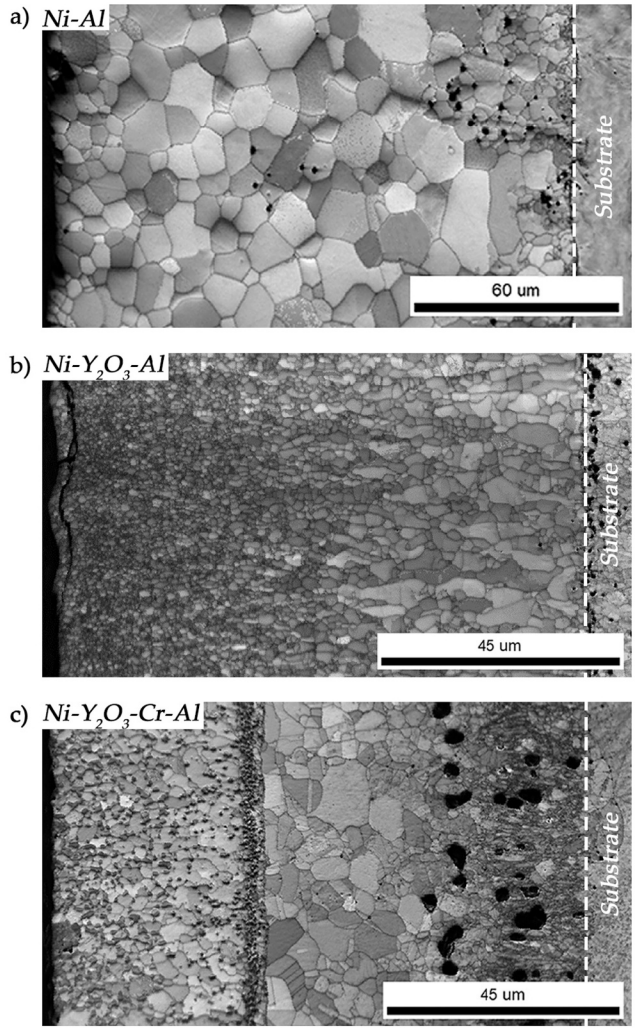

Fig. 6. EBSD band contrast images of surface cross-sections of: a) Ni-Al, b) Ni-Y_2O_3-Al and c) Ni-Y_2O_3-Cr-Al coatings after pack cementation.

interdiffusion during oxidation at 1100 °C. The nearly continuous layer of pores ultimately resulted in an almost complete detachment of the coating at the substrate-coating interface. Consequently, this detachment led to the oxidation of both the substrate and the delaminated surfaces, contributing significantly to a substantial increase in mass during oxidation, as depicted in Fig. 11b. Additionally, the inward diffusion of aluminum was restricted as the coating lost contact with the substrate. In contrast, the Ni-Y_2O_3-Al coating shown in Fig. 12b exhibited no signs of spallation or delamination effects, nor did it display Kirkendall voids. Similar observations were found in Ni-Y_2O_3-Cr-Al coatings (Fig. 13b), which also showed an absence of spallation and delamination effects. However, in the case of Ni-Y_2O_3-Cr-Al coatings, Kirkendall voids were not completely mitigated but were noticeably reduced in both quantity and size.

As previously discussed, the Y_2O_3 particles likely hinder the inward grain boundary diffusion of aluminum, delaying the onset of the β-γ′-phase transformation and reducing the formation of voids [41,43]. The second contributing factor in this transformation is the diffusion of Ni into the coating, a process that tends to increase at higher oxidation temperatures. Ni diffusion plays a significant role in the formation of Kirkendall voids, much like Al. At a temperature as high as 1100 °C, Ni diffusion is expected to be particularly dominant, and the presence of Y_2O_3 particles effectively reduces this phenomenon. This reduction in phase transformation and void formation, in turn, enhances the adherence of the coating. In the case of the Ni-Cr-Al coating, as illustrated in Fig. 13a, a substantial portion of the layer transitioned into the γ-phase, with some thin regions of the γ′-phase remaining beneath the outer Al_2O_3 scale. As evidenced by the elemental concentration line scan presented in Fig. 13a, a noticeable depletion of aluminum is observed in the subsurface region. This loss of aluminum can be attributed to both oxide spallation and inward diffusion processes. In contrast, the elemental profile of the Ni-Y_2O_3-Cr-Al coating containing nanoparticles (Fig. 13b) reveals the presence of yttria within the Al_2O_3 scale. This presence of yttria contributes to a "template" effect for enhanced α-Al_2O_3 formation [54] due to their similar crystallographic structures and an enhanced adhesion of the oxide scale, resulting in an overall improvement in oxidation resistance and a parabolic growth of the oxide scale. Furthermore, high concentrations of Y_2O_3 (Fig. 13b) were again observed at the coating-substrate interface, indicating the presence of a diffusion barrier effect for aluminum.

3.5. Hot corrosion resistance

As demonstrated in the previous section, IN617 lacks sufficient resistance against cyclic oxidation at 1100 °C and thus should be coated for industrial application at this temperature. Colder parts of turbine blades normally fall in the temperature region where type II hot corrosion occurs. Type II hot corrosion refers to a high-temperature oxidation and sulfidation process that occurs in the presence of molten salts at

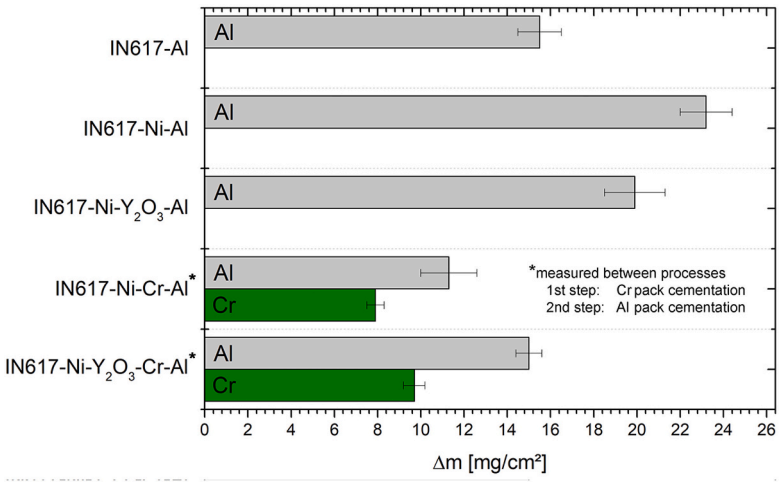

Fig. 7. Comparison of the absolute mass changes for different coatings after pack cementation carried out for the same deposition parameters.

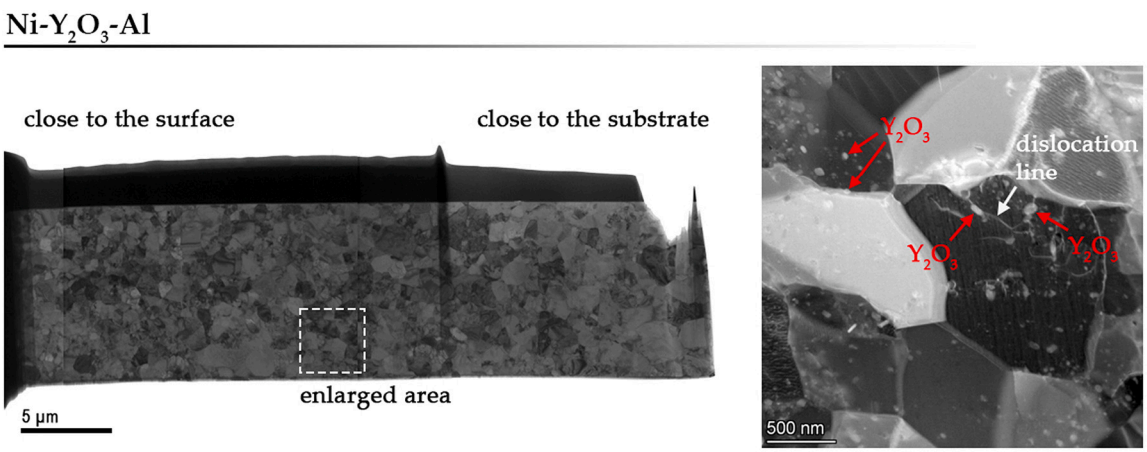

Fig. 8. Bright field image of a Ni-Y_2O_3-Al TEM lamella with an enlarged region shown by a STEM-HAADF image. The HAADF image was acquired with collection angles allowing enhancement of the visibility of the yttria nanoparticles and grain boundaries within the coating.

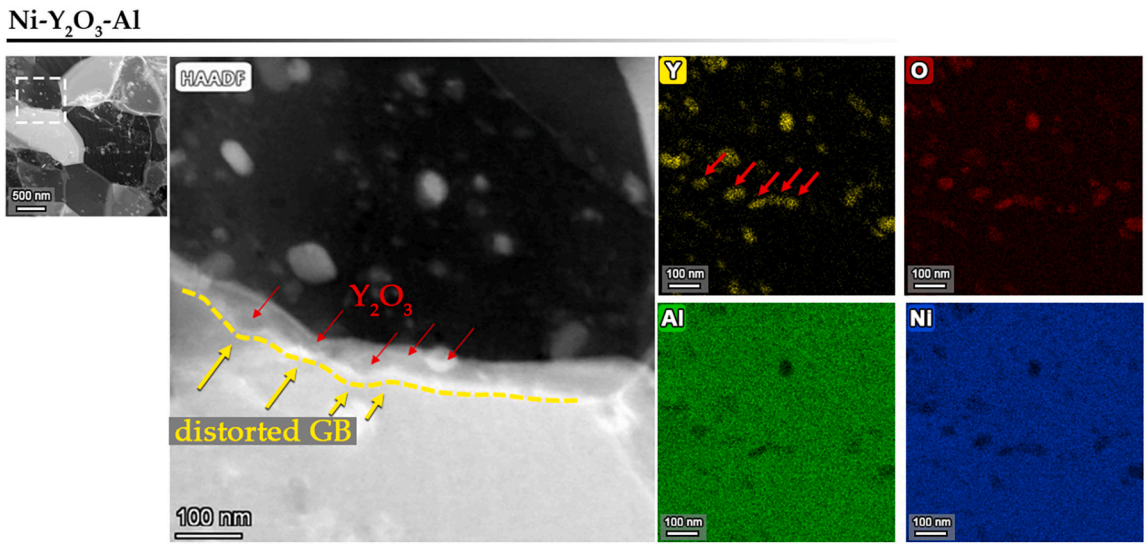

Fig. 9. STEM-HAADF image of a grain boundary in a Ni-Y_2O_3-Al coating. The grain boundary (yellow line) is close to an edge-on position so the overlap of the grain boundary and yttria signal suggests that the yttria particles are at or in proximity to the grain boundary. Multiple Y_2O_3 particles are located at a twisted grain boundary, showing the grain boundary pinning effect of the particles. (For interpretation of the references to color in this figure legend, the reader is referred to the web version of this article.)

elevated temperatures in gas turbines. It involves the formation of sulfate deposits on the turbine components, leading to degradation and corrosion of materials, particularly in areas where the turbine blades experience colder temperatures. Coatings applied to these blades must be resilient enough to withstand this specific type of corrosive attack caused by the combination of high temperatures and reactive salts. Since Ni and Al show the lowest solubility in Na_2SO_4 at different Na_2O activities, a synergistic effect between the acidic dissolution of nickel oxide and the basic dissolution of alumina and chromia occurs, accelerating the hot corrosion attack [8,55]. Furthermore, Mo within the alloy tends to form acidic MoO_3 under hot corrosion conditions, causing alloy-induced fluxing of the other oxides [56].

Aluminum diffusion coatings on IN617, as shown in Fig. 14, led to a reduction in sulphate-vanadate corrosion resistance when compared to plain IN617. Due to the surface enrichment of aluminum for IN617-Al, the available chromium was reduced which has been shown to lower the hot corrosion resistance caused by sulfur-containing compounds [57–59]. The wetting behaviors of IN617 and IN617-Al by the molten ash mixture were different when compared to the other coatings, leading to thinner ash layers on IN617 and IN617-Al. Generally thick ash layers lead to higher corrosion attack than thin ash layers [60] due to a higher partial pressure of sulfur at the contact zone between the ash and the metal. Thus, the hot corrosion attack of IN617 and IN617-Al would be even higher under comparable ash layer thicknesses as the other nanoparticle MMC coatings.

The ash coverage on the galvanically deposited coatings was thicker and comparable between the Ni-Y_2O_3-Al and Ni-Y_2O_3-Cr-Al coatings as well as for the particle-free control samples. For these thicker ash coverages on the samples, the corrosion was generally dominated by sulfur attack, leading to higher corrosion loss, as shown in the cumulative probability plot [27–29,61–64] in Fig. 14. Even though the corrosion loss for IN617 with a thicker and comparable ash deposit is expected to be somewhat higher, a direct comparison between the Ni-Y_2O_3-Cr-Al coating and plain IN617 revealed an overall comparable corrosion loss (Fig. 14b). Generally, both coatings with yttria particles present in the metallic matrix revealed better hot corrosion resistance than their particle-free counterparts but were not able to match the intrinsically high hot corrosion resistance of IN617. Cross-sections of the hot-corroded Ni—Al and Ni-Y_2O_3-Al coatings (Fig. 15) revealed that the Ni—Al coating (Fig. 15a) was strongly attacked by sulfur, transforming

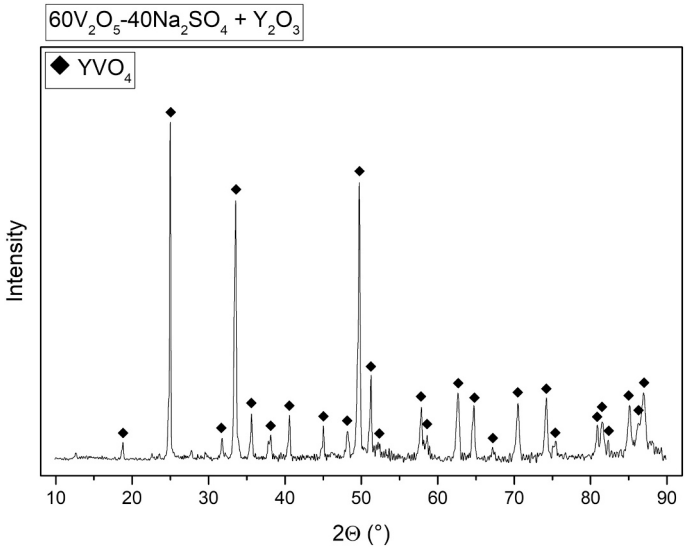

Fig. 10. X-ray diffractogram of a $60V_2O5\text{-}40Na_2SO_4$ ash mixture with Y_2O_3 after exposure to 700 °C for 50 h in a synthetic air +0.1 % SO_2 atmosphere. Note that Y_2O_3 was added stoichiometrically based on the V_2O_5 content of the ash.

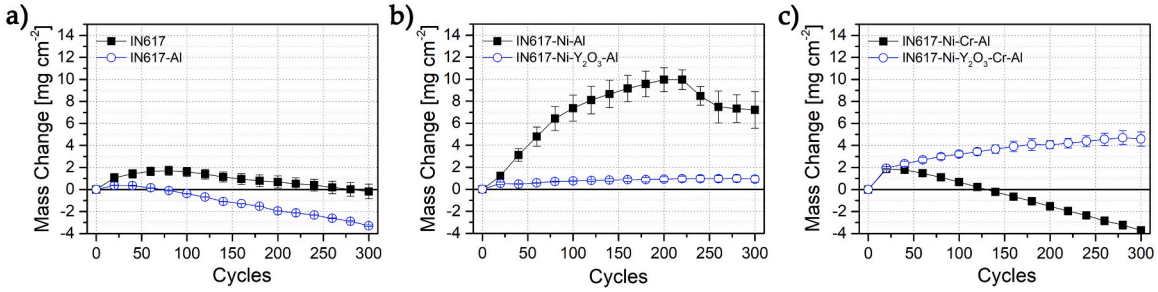

Fig. 11. Net mass changes for cyclic oxidation in air at 1100 °C (67 min HT, 15 min PAC) of a) uncoated IN617 and IN617-Al, b) Ni-Al and Ni-Y_2O_3-Al, and c) Ni-Cr-Al and Ni-Y_2O_3-Cr-Al coatings on IN617.

the dense coating into a porous structure, through which the diffusion of sulfur was likely enhanced.

The corrosive attack led to an almost complete delamination of the remaining coating for the unmodified aluminide. In areas where the β-phase was fully consumed, the attack was rapid and lateral spreading of the corrosive reaction front occurred, leading to complete loss of protective properties. The Ni-Y_2O_3-Al (Fig. 15b) maintained the protective properties of the coating for ~30 % of the sample surface. Additionally, most of the β-phase was sustained, indicating a reduced loss of Al due to inward diffusion and oxide dissolution. When the molten salt reached the coating layer rich in yttria, which was observed for 70 % of the coating surface, no further attack could be observed. A measurable impact of the yttria on vanadium oxide could not be observed since vanadium mostly remained at the ash surface for both Ni—Al coatings. The main yttria influence is in the grain refining effect, not only reducing the formation of Kirkendall voids and inward diffusion of Al, but also limiting sulfur inward diffusion. Although grain boundaries typically increase diffusion, the presence of particles along these grain boundaries actually impedes the process by decreasing the vacancy concentration. The resulting slower sulfur attack prevented degradation of the coating into a porous, non-protective layer, which was observed to be the main attack mechanism for the particle-free coatings.

As can be seen from Fig. 16a, the vanadate hot corrosion attack on the Ni-Cr-Al coating led to a comparable porous structure as already described for the Ni—Al coating, forming internal NiS and Al_2O_3. The corrosion products in the ashes were homogenously distributed, indicating a rapid corrosion attack with no intermediate protective oxides present. The Ni-Y_2O_3-Cr-Al coating Fig. 16b, in contrast, showed a layered structure of different corrosion products. The predominant elements in those layers changed, indicating alternating scale formation and then oxide dissolution.

While the pore formation in the remaining coating was minimized due to slower interdiffusion, the corrosion attack of the molten salts was also slowed down by the Cr-rich, Al-rich and Y-rich zone. The yttria particles also limited inward diffusion of sulfur through the grain boundaries, preventing internal sulfidation [43]. The influence of yttria nanoparticles on the coating morphology and chemistry is complex. While further optimization of the coatings is required, the feasibility and benefit of incorporating yttria nanoparticles to improve oxidation and corrosion resistance was clearly demonstrated in this study.

4. Conclusions

Yttria was successfully co-deposited in a high amount from a chloride-free nickel sulfamate bath using insoluble DSA anodes and ultrasonic mixing. The Y_2O_3 nanoparticles resulted in significant grain refinement of the coating after Al enrichment by pack cementation. The distribution of nanoparticles in the coating was shown to be strongly dependent on the activity of the diffusing element, resulting in homogenous particle distribution throughout the entire coating thickness for high activity coatings (Al) and a particle-free layer in the surface region for low activity coatings (Cr). Yttria nanoparticles were located within the grains and at the grain boundaries. Nanoparticles at the grain

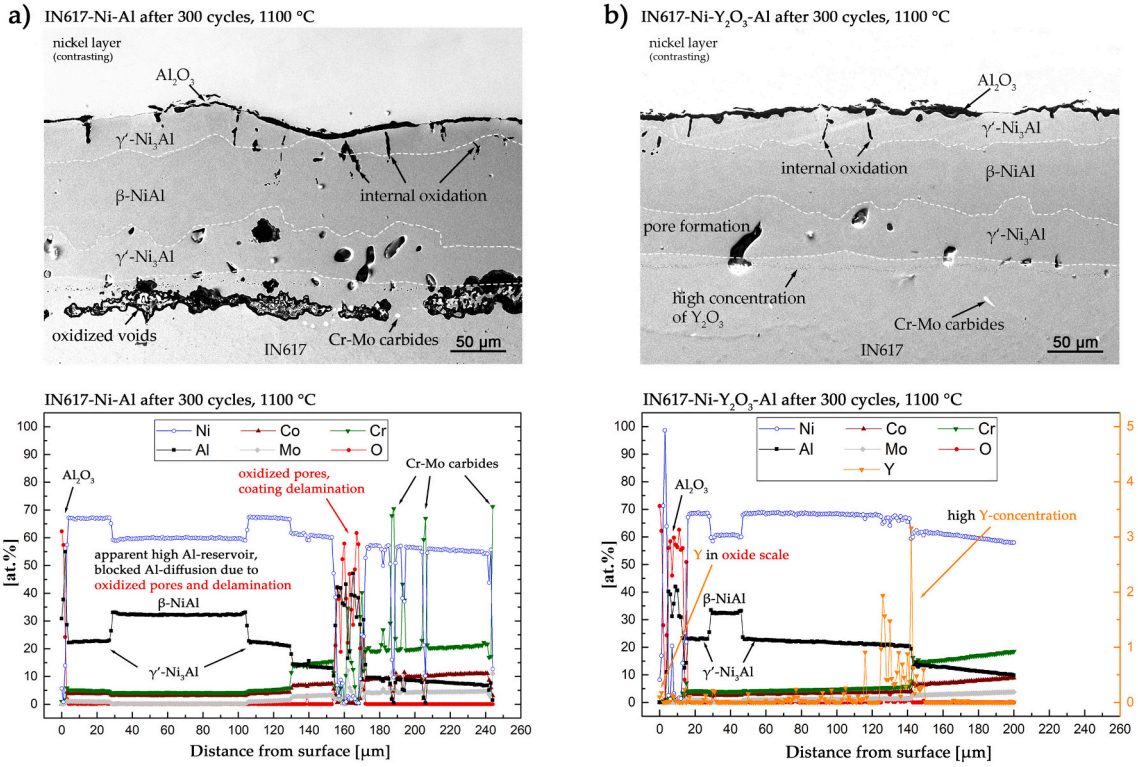

Fig. 12. SEM-BSE cross-sectional images and comparison of the phase distributions between a) Ni-Al and b) Ni-Y_2O_3-Al and respective EDS line-scans after 300 cycles of cyclic oxidation at 1100 °C. Dashed lines indicate the phase transitions.

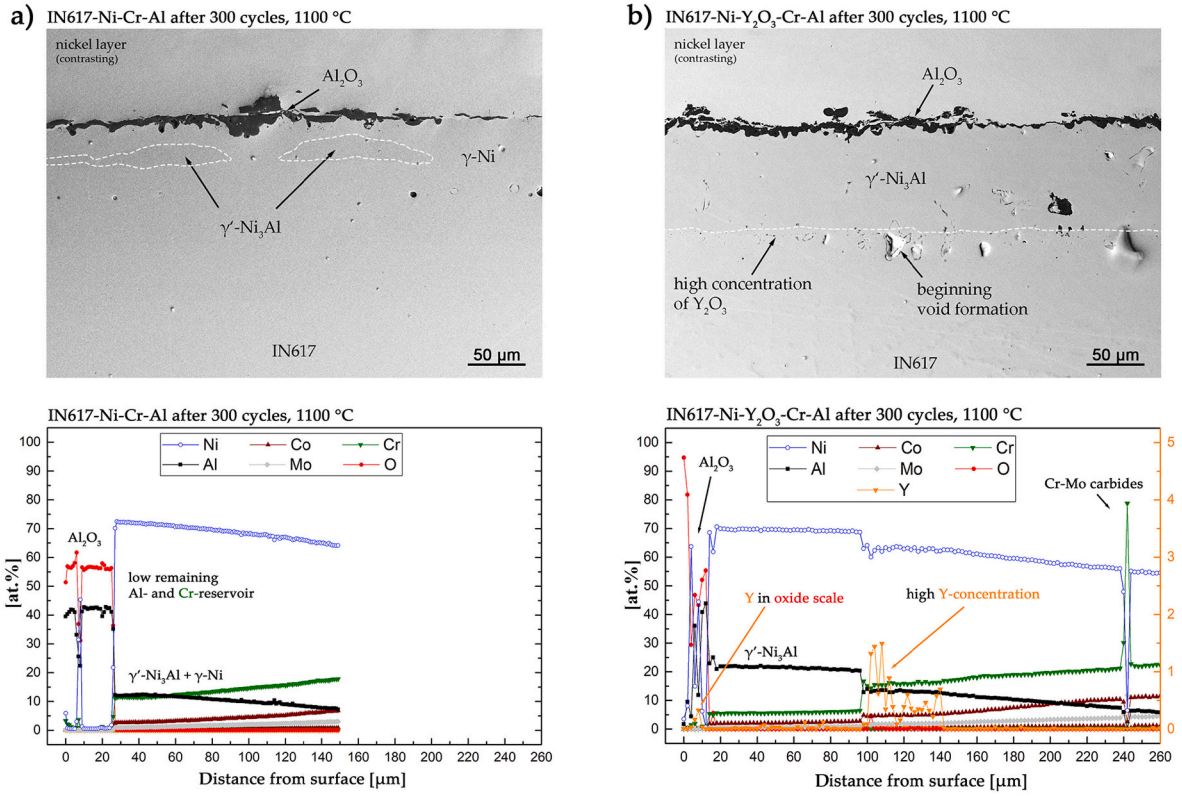

Fig. 13. SEM-BSE cross-sectional image and comparison of the phase distribution between a) Ni-Cr-Al and b) Ni-Y_2O_3-Cr-Al and respective EDS line-scans after 300 cycles of cyclic oxidation at 1100 °C. Dashed lines indicate the phase transitions.

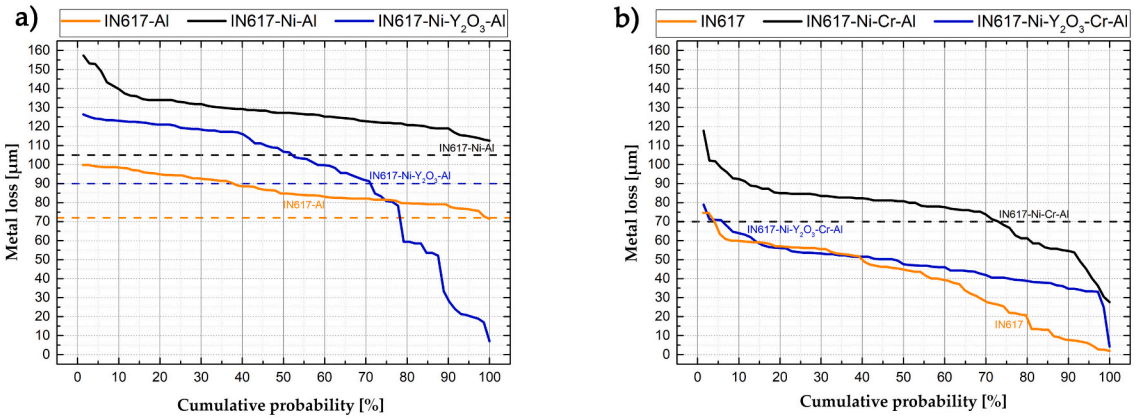

Fig. 14. Cumulative probability plots of a) Al-diffusion coatings and b) Cr-Al-diffusion coatings and the base material IN617 after corrosion testing at 700 °C for 50 h with a 30 mg/cm^2 ash cover consisting of 60V_2O_5-40Na_2SO_4. The dashed lines indicate the substrate/coating interface of the respective coatings. Note that no substrate/coating interface is available for the unmodified IN617.

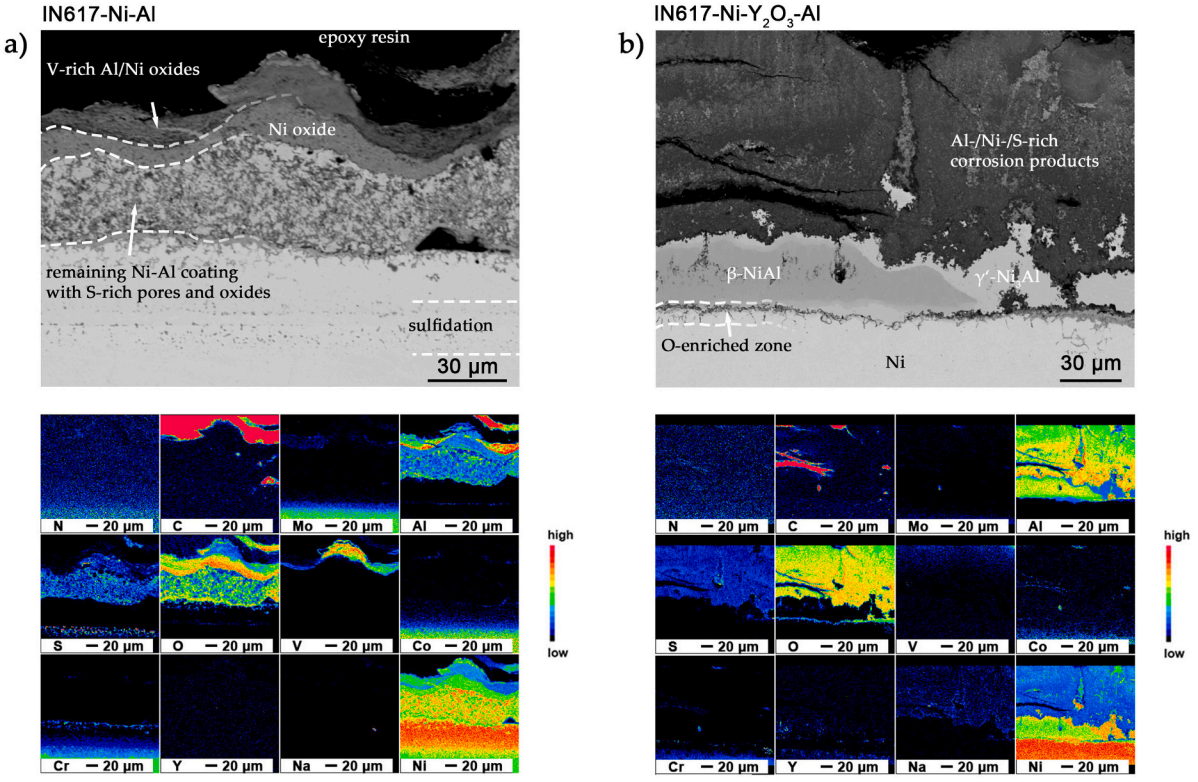

Fig. 15. SEM-BSE images of the a) Ni-Al and b) Ni-Y_2O_3-Al coatings on IN617 after exposure at 700 °C for 50 h with a 30 mg/cm^2 ash cover consisting of 60V_2O_5-40Na_2SO_4 with the respective EPMA element maps.

boundaries resulted in the distortion of these boundaries and facilitated a significant grain refinement, while within the grains, these particles induced the formation of dislocation bands.

The overall uptake of elements from the pack cementation process was significantly influenced by the nanoparticles in the electroplated Ni matrix. Aluminum inward diffusion during pack cementation was reduced due to grain boundary yttria nanoparticles lowering Al inward diffusion. In the case of chromium diffusion into the Ni-Y_2O_3 coating, these nanoparticles played a dual role: they reduced void formation and facilitated enhanced outward diffusion of nickel, which consequently led to a greater uptake of chromium.

Ni-Y_2O_3-Al and Ni-Y_2O_3-Cr-Al MMC coatings have been shown to have higher oxidation resistance at 1100 °C and higher vanadate hot corrosion resistance than their particle-free counterparts. For both environmental conditions, the particles reduced interdiffusion and inhibited the formation of pores. Both particle-containing coatings significantly improved the cyclic oxidation resistance.

The coatings developed in this study present a promising solution for high-temperature corrosion and oxidation protection, while simultaneously acting as an efficient diffusion barrier. The cost-effectiveness and adaptability of the coating elements and particles, compared to traditional deposition methods such as High-Velocity Oxygen Fuel (HVOF) or Atmospheric Plasma Spraying (APS), underscore their potential for widespread industrial application.

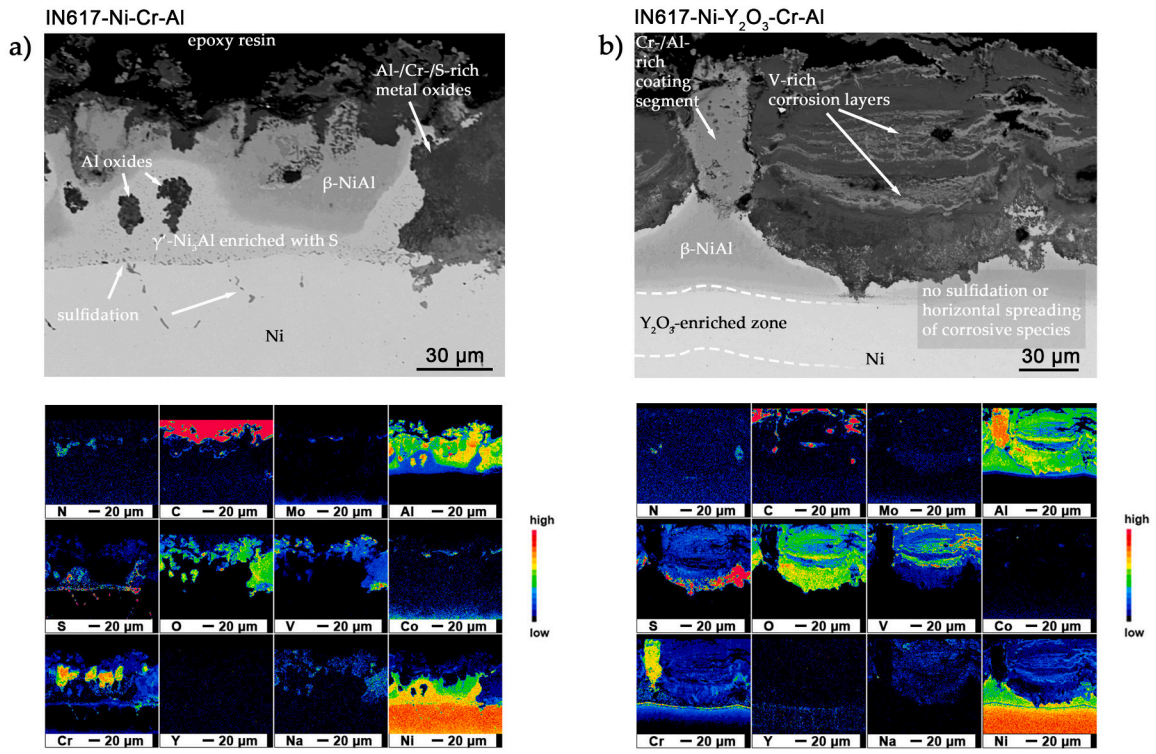

Fig. 16. SEM-BSE images of the a) Ni-Cr-Al and b) Ni-Y_2O_3-Cr-Al coatings on IN617 after exposure at 700 °C for 50 h with a 30 mg/cm^2 ash cover consisting of 60V_2O_5-40Na_2SO_4 with the respective EPMA element maps.

CRediT authorship contribution statement

Christoph Grimme: Writing – original draft, Visualization, Validation, Project administration, Methodology, Investigation, Data curation, Conceptualization. **Kan Ma:** Writing – review & editing, Visualization, Investigation, Data curation. **Robin Kupec:** Methodology, Investigation. **Ceyhun Oskay:** Writing – review & editing. **Emma M.H. White:** Writing – review & editing. **Alexander J. Knowles:** Supervision, Funding acquisition. **Mathias C. Galetz:** Supervision, Funding acquisition, Conceptualization.

Declaration of competing interest

The authors declare that they have no known competing financial interests or personal relationships that could have appeared to influence the work reported in this paper.

Data availability

Data will be made available on request.

Acknowledgements

The German Research Foundation (DFG) is gratefully acknowledged for supporting this project under contract GA1704/8-1. The authors would like to thank Dr. Gerald Schmidt and Melanie Thalheimer for performing EPMA and EBSD measurements and Mathias Röhrig for technical support. This project has received funding from the European Union's Horizon 2020 - Research and Innovation Framework Programme under grant agreement No 958418, through the "COMPASsCO2" project (https://www.compassco2.eu). Alexander Knowles acknowledges support from: UKRI Future Leaders Fellowship (MR/T019174/1) and Royal Academy of Engineering Research Fellowship (RF\201819\18\158). The authors thank the Centre for Electron Microscopy (University of Birmingham) for their support & assistance in this work.

References

[1] S.K. Gupta, Low-grade fuel engines in the United States, Marine Technology and SNAME News 22 (1985) 179–187, https://doi.org/10.5957/mt1.1985.22.2.179.
[2] J.A. Goebel, F.S. Pettit, G.W. Goward, Mechanisms for the hot corrosion of nickel-base alloys, Metall. Trans. A. 4 (1973) 261–278.
[3] R.A. Rapp, Hot corrosion of materials: a fluxing mechanism? Corros. Sci. 44 (2002) 209–221.
[4] R.A. Rapp, K.S. Goto, The hot corrosion of metals by molten salts, in: R. Selman, J. Braunstein (Eds.), Second International Symposium on Molten Salts, Electrochemical Society, 1981, pp. 159–177.
[5] A.J. Knowles, L. Reynolds, V.A. Vorontsov, D. Dye, A nickel based superalloy reinforced by both Ni3Al and Ni3V ordered-fcc precipitates, Scr. Mater. 162 (2019) 472–476, https://doi.org/10.1016/j.scriptamat.2018.12.013.
[6] N.S. Bornstein, Vanadium Corrosion Studies, 1993.
[7] P. Hancock, Vanadic and chloride atack of superalloys, Mater.Sci.Technol. 3 (1987) 536–544.
[8] N. Otsuka, Fireside corrosion, in: Shreir's Corrosion, Elsevier, Amsterdam, 2010, pp. 457–481.
[9] X. Montero, M.C. Galetz, Inhibitors and coatings against vanadate-containing oil ash corrosion of boilers, Surf. Coat. Technol. 304 (2016) 211–221.
[10] W.R. May, M.J. Zetlmeisl, L. Bsharah, R.R. Annand, High-temperature corrosion in gas turbines and steam boilers by fuel impurities. III. Evaluation of magnesium as a corrosion inhibitor, Ind. Eng. Chem. Prod. Res. Dev. 12 (1973) 145–149.
[11] C. Soares, Gas Turbines: A Handbook of Air, Land and Sea Applications, Second edition, Butterworth-Heineman, Oxford, U.K, 2015.
[12] Y. Zhang, Electrodeposited MCrAlY coatings for gas turbine engine applications, JOM 67 (2015) 2599–2607, https://doi.org/10.1007/s11837-015-1640-0.
[13] I. Gurrappa, Identification of hot corrosion resistant MCrAlY based bond coatings for gas turbine engine applications, Surf. Coat. Technol. 139 (2001) 272–283.
[14] J.R. Nicholls, N.J. Simms, W.Y. Chan, H.E. Evans, Smart overlay coatings — concept and practice, Surf. Coat. Technol. 149 (2002) 236–244, https://doi.org/10.1016/S0257-8972(01)01499-2.
[15] G.W. Goward, Progress in coatings for gas turbine airfoils, Surf. Coat. Technol. 108-109 (1998) 73–79.
[16] F. Ebadi, F. Shahriari Nogorani, F. Fatemi, The inhibiting effect of reactive element oxides on the pack cementation aluminide coating formation, Metall and Mat Trans A 51 (2020) 5958–5964, https://doi.org/10.1007/s11661-020-05973-0.
[17] M. Fichera, R. Leonardi, C.A. Farina, Fuel ash corrosion and its prevention with MgO addition, Electrochim. Acta 32 (1987) 955–960, https://doi.org/10.1016/0013-4686(87)87089-5.

[18] T.W. Jelinek, Praktische Galvanotechnik: Ein Lehr- und Handbuch; mit 96 Tabellen im Text, einem speziellen Tabellen-Anhang und einer Übersicht "Chemikalien für die Galvanotechnik", seventh., aktualisierte Aufl., Leuze, Bad Saulgau, 2013.
[19] N.V. Mandich, D.W. Baudrand, Troubleshooting electroplating installations: nickel sulfamate plating systems, Plat. Surf. Finish. 89 (2002) 68–76.
[20] H. Schwegmann, A.J. Feitz, F.H. Frimmel, Influence of the zeta potential on the sorption and toxicity of iron oxide nanoparticles on S. cerevisiae and E. coli, J. Colloid Interface Sci. 347 (2010) 43–48, https://doi.org/10.1016/j.jcis.2010.02.028.
[21] A. Hovestad, L.J.J. Janssen, Electroplating of metal matrix composites by codeposition of suspended particles, in: B.E. Conway, M.E. Gamboa-Adelco, C. G. Vayenas, R.E. White (Eds.), Modern Aspects of Electrochemistry, Springer Science + Business Media Inc, Boston, MA, 2005, pp. 475–532.
[22] S. Erdei, G.G. Johnson, F.W. Ainger, Growth studies of YVO4 crystals (II). Changes in YVO-stoichiometry, Cryst. Res. Technol. 29 (1994) 815–828, https://doi.org/10.1002/crat.2170290610.
[23] S.C. Santos, L. Setz, C. Yamagata, S.R.H. de Mello-Castanho, Rheological study of yttrium oxide aqueous suspensions, Mater. Sci. Forum 660-661 (2010) 712–717, https://doi.org/10.4028/www.scientific.net/MSF.660-661.712.
[24] K. Cai, B. Román-Manso, J.E. Smay, J. Zhou, M.I. Osendi, M. Belmonte, P. Miranzo, Geometrically complex silicon carbide structures fabricated by robocasting, J. Am. Ceram. Soc. 95 (2012) 2660–2666, https://doi.org/10.1111/j.1551-2916.2012.05276.x.
[25] F. La Lumia, L. Ramond, C. Pagnoux, G. Bernard-Granger, Preparation and co-dispersion of TiO2-Y2O3 suspensions through the study of their rheological and electrokinetic properties, Ceram. Int. 45 (2019) 3023–3032, https://doi.org/10.1016/j.ceramint.2018.10.123.
[26] ISO 13573: Corrosion of metals and alloys - test method for thermal cycling exposure testing under high temperature corrosion conditions for metallic materials, ISO TC156 WG 13 (High Temperature Corrosion), 2012.
[27] X. Montero, I. Demler, V. Kuznetsov, M.C. Galetz, Factors governing slurry aluminization of steels, Surf. Coat. Technol. 309 (2017) 179–186.
[28] T.A. Kircher, B.G. McMordie, A. McCarter, Performance of a silicon-modified aluminide coating in high temperature hot corrosion test conditions, Surf. Coat. Technol. 68 (1994) 32–37.
[29] S.A. Azarmehr, K. Shirvani, A. Solimani, M. Schütze, M.C. Galetz, Effects of Pt and Si on the low temperature hot corrosion of aluminide coatings exposed to Na2SO4-60 mol% V2O5 salt, Surf. Coat. Technol. 362 (2019) 252–261, https://doi.org/10.1016/j.surfcoat.2019.01.116.
[30] B. Wielage, T. Lampke, M. Zacher, D. Dietrich, Electroplated nickel composites with micron- to nano-sized particles, High-Performance Ceramics IV 384 (2008) 283–309, https://doi.org/10.4028/www.scientific.net/KEM.384.283.
[31] F. Xia, M. Wu, F. Wang, Z. Jia, A. Wang, Nanocomposite Ni–TiN coatings prepared by ultrasonic electrodeposition, Curr. Appl. Phys. 9 (2009) 44–47, https://doi.org/10.1016/j.cap.2007.11.014.
[32] T. Lampke, B. Wielage, D. Dietrich, A. Leopold, Details of crystalline growth in co-deposited electroplated nickel films with hard (nano)particles, Appl. Surf. Sci. 253 (2006) 2399–2408, https://doi.org/10.1016/j.apsusc.2006.04.060.
[33] F. Xia, W. Jia, C. Ma, J. Wang, Synthesis of Ni–TiN composites through ultrasonic pulse electrodeposition with excellent corrosion and wear resistance, Ceram. Int. 44 (2018) 766–773, https://doi.org/10.1016/j.ceramint.2017.09.245.
[34] B. Grushko, W. Kowalski, D. Pavlyuchkov, B. Przepiorzynski, M. Surowiec, A contribution to the Al-Ni-Cr phase diagram, J. Alloys Compd. 460 (2008) 299–304.
[35] W. Huang, Y.A. Chang, Thermodynamic properties of the Ni-Al-Cr system, Intermetallics 7 (1999) 863–874.
[36] B. Grégoire, G. Bonnet, F. Pedraza, Development of a new slurry coating design for the surface protection of gas turbine components, Surf. Coat. Technol. 374 (2019) 521–530.
[37] Y.C. Lee, A.K. Dahle, D.H. StJohn, The role of solute in grain refinement of magnesium, Metall and Mat Trans A 31 (2000) 2895–2906, https://doi.org/10.1007/bf02830349.
[38] H. Jiang, Y. Song, L. Zhang, J. He, S. Li, J. Zhao, Efficient grain refinement of Al alloys induced by in-situ nanoparticles, J. Mater. Sci. Technol. 124 (2022) 14–25, https://doi.org/10.1016/j.jmst.2021.12.077.
[39] M. Easton, D. StJohn, Grain refinement of aluminum alloys: part I. The nucleant and solute paradigms—a review of the literature, Metall and Mat Trans A 30 (1999) 1613–1623, https://doi.org/10.1007/s11661-999-0098-5.
[40] H.M. Fu, M.-X. Zhang, D. Qiu, P.M. Kelly, J.A. Taylor, Grain refinement by AlN particles in Mg–Al based alloys, J. Alloys Compd. 478 (2009) 809–812, https://doi.org/10.1016/j.jallcom.2008.12.029.
[41] J. Jaseliunaite, A. Galdikas, Kinetic modeling of grain boundary diffusion: the influence of grain size and surface processes, Materials (Basel) 13 (2020), https://doi.org/10.3390/ma13051051.
[42] M.M.P. Janssen, Diffusion in the nickel-rich part of the Ni-Al system at 1000° to 1300°C, Ni_3Al layer growth, diffusion coefficients and interface concentrations, Metall. Trans. A. 4 (1973) 1623–1633.
[43] C. Geers, I. Panas, Impact of grain boundary density on oxide scaling revisited, High Temperature Corrosion of Mater. 91 (2019) 55–75, https://doi.org/10.1007/s11085-018-9867-0.
[44] R.J. Christensen, V.K. Tolpygo, D.R. Clarke, The influence of the reactive element yttrium on the stress in alumina scales formed by oxidation, Acta Mater. 45 (1997) 1761–1766.
[45] Z. Chen, S. Speakman, J. Howe, H. Wang, W. Porter, R. Trice, Investigation of reactions between vanadium oxide and plasma-sprayed yttria-stabilized zirconia coatings, J. Eur. Ceram. Soc. 29 (2009) 1403–1411.
[46] W. Przybilla, M. Schütze, Growth stresses in the oxide scales on TiAl alloys at 800 and 900°C, Oxid. Met. 58 (2002) 337–359.
[47] M. Schütze, D.R. Holmes, R.B. Waterhouse, Protective Oxide Scales and Their Breakdown, Wiley Chichester, 1997.
[48] B.A. Pint, Y. Zhang, Performance of Al-rich oxidation resistant coatings for Fe-base alloys, Mater. Corros. 62 (2011) 549–560, https://doi.org/10.1002/maco.201005884.
[49] P. Ganesan, G.D. Smith, D.H. Yates, Performance of Inconel alloy 617 in actual and simulated gas turbine environments, Mater. Manuf. Process. 10 (1995) 925–938, https://doi.org/10.1080/10426919508935080.
[50] C. Oskay, M. Rudolphi, E.E. Affeldt, M. Schütze, M.C. Galetz, Evolution of microstructure and mechanical properties of NiAl-diffusion coatings after thermocyclic exposure, Intermetallics 89 (2017) 22–31.
[51] S.K. Sharma, G.D. Ko, F.X. Li, K.J. Kang, Oxidation and creep failure of alloy 617 foils at high temperature, J. Nucl. Mater. 378 (2008) 144–152.
[52] D. Kim, C. Jang, W.S. Ryu, Oxidation characteristics and oxide layer evolution of alloy 617 and Haynes 230 at 900 °C and 1100 °C, High Temperature Corrosion of Mater. 71 (2009) 271–293, https://doi.org/10.1007/s11085-009-9142-5.
[53] C. Jang, D. Lee, D. Kim, Oxidation behaviour of an Alloy 617 in very high-temperature air and helium environments, Int. J. Press. Vessel. Pip. 85 (2008) 368–377, https://doi.org/10.1016/j.ijpvp.2007.11.010.
[54] X. Peng, Y. Huang, X. Wang, Y. Xie, Nanoparticles application in promoting the growth of a more protective oxide scale at high temperatures, High Temperature Corrosion of Mater. (2023) 1–38, https://doi.org/10.1007/s11085-023-10185-z.
[55] R.A. Rapp, Chemistry and electrochemistry of the hot corrosion of metals, Corr 42 (1986) 568–577.
[56] B.S. Lutz, J.M. Alvarado-Orozco, L. Garcia-Fresnillo, G.H. Meier, Na2SO4-deposit-induced corrosion of Mo-containing alloys, Oxid. Met. 88 (2017) 599–620.
[57] S. Shih, Y. Zhang, X. Li, Sub-melting point hot corrosion of alloys and coatings, Mater. Sci. Eng. A 120 (1989) 277–282.
[58] M.W. Dust, Effect of chromium addition to the low temperature hot corrosion resistance of platinum modified aluminide coatings. 0, 1985.
[59] N. Eliaz, G. Shemesh, R.M. Latanision, Hot corrosion in gas turbine components, Eng. Fail. Anal. 9 (2002) 31–43.
[60] B. Grégoire, X. Montero, M.C. Galetz, G. Bonnet, F. Pedraza, Mechanisms of hot corrosion of pure nickel at 700°C: influence of testing conditions, Corros. Sci. 141 (2018) 211–220, https://doi.org/10.1016/j.corsci.2018.06.009.
[61] X. Montero, M.C. Galetz, M. Schütze, Sulphidation behavior of a non harmful water-based Al and Al-Si slurry coating on CM247 superalloy, Oxid. Met. 80 (2013) 635–649, https://doi.org/10.1007/s11085-013-9412-0.
[62] X. Montero, M.C. Galetz, Effect of different vanadate salt composition on oil ash corrosion of boilers, Oxid. Met. 89 (2018) 395–414.
[63] A. Encinas-Oropesa, G.L. Drew, M.C. Hardy, A.J. Leggett, J.R. Nicholls, N.J. Simms, Effects of oxidation and hot corrosion in a nickel disc alloy, in: Superalloys 2008, TMS, Warrendale, Pa, 2008, pp. 609–618.
[64] J. Sumner, A. Encinas-Oropesa, N.J. Simms, J.R. Nicholls, Type II hot corrosion: kinetics studies of CMSX-4, High Temperature Corrosion of Mater. 80 (2013) 553–563, https://doi.org/10.1007/s11085-013-9395-x.